Research Article Vol. 4, No. 8 / August 2017 / Optica 839

Tunable transformation optical waveguide bends in liquid

Hai L. Liu,[1,†] Xiao Q. Zhu,[1,†] Li Liang,[1] Xu M. Zhang,[2] and Yi Yang[1,*]

[1]Key Laboratory of Artificial Micro- and Nano-structures of Ministry of Education, School of Physics & Technology, Wuhan University, Wuhan 430072, China
[2]Department of Applied Physics, Hong Kong Polytechnic University, Hung Hom, Kowloon, Hong Kong
*Corresponding author: yangyiys@whu.edu.cn

Received 11 May 2017; accepted 15 June 2017 (Doc. ID 295811); published 25 July 2017

Optical waveguide bends are indispensable to integrated optical systems, and many methods to mitigate bend loss have thus been proposed. Transformation optics (TO) causes light to travel around a bend as if it was propagating in a straight waveguide, eliminating the bend loss. Many reported TO waveguide bends have utilized solid materials, but there are fundamental difficulties for real applications because of their complex fabrication, lack of reconfiguration, and the so-called effective medium condition. Here, we develop a method to overcome these problems using the convection–diffusion of liquids. It enables real-time tunable transformation optical waveguide bends using natural liquid diffusion while still exhibiting the major merits of quasi-conformal mapping. We have experimentally demonstrated bending in visible light by 90 and 180° while preserving the intensity profile at a reasonably high level of fidelity. This work bridges fluid dynamics and optics and has the potential for application in on-chip biological, chemical, and biomedical measurements, as well as detectors and tunable optical systems.

OCIS codes: (160.2710) Inhomogeneous optical media; (230.3990) Micro-optical devices; (230.3120) Integrated optics devices.

https://doi.org/10.1364/OPTICA.4.000839

1. INTRODUCTION

Transformation optics (TO) is a new method of designing devices that can manipulate light through modification of electromagnetic space. Unlike traditional TO methods that require media with anisotropy and inhomogeneity properties [1,2], quasi-conformal TO (QCTO) provides a relatively simple solution by using only isotropic media [3–7]. Both methods show great potential for unprecedented devices such as cloaks [1,2,4,6], conformal antennas [8], gravitational lens mimicking [9], Luneberg lenses [10], and waveguide bends [11–18].

Among them, a waveguide bend is an indispensable component in integrated optical systems [12]. Transformation waveguide bends can inherently make light to travel along a bend channel as if it was propagating in a straight waveguide, showing its good performance characteristic. However, many previous TO bend studies have been merely concepts or lab curiosity experiments because of the requirement of a continuous material relative to the working wavelength. Examples include anisotropic complex media designs at centimeter wavelengths [11,12], anisotropic metamaterial designs at THz [13] and centimeter wavelengths [14], and isotropic materials at microwave wavelengths [15,16]. In addition, only two experimental results have so far been presented [17,18]. One used metamaterials at microwave wavelengths [17] and the other employed a silicon waveguide with a varying cross-section profile to operate at 1.55 μm [18].

Optofluidics shows powerful potential for optical tunable devices [19–31] such as optofluidic microlenses [27], optofluidic light switches [29], tunable reflectors [21], detection systems [22,30,31], and liquid waveguides [20,25,26]. One of the special merits of optofluidics is the ability to use the liquid diffusion process to generate a gradient refractive index (RI) profile, which is inherent in isotropic media and naturally suitable for QCTO [7]. This inspired us to develop optofluidic waveguide bends.

In this work, we employ the diffusion process to demonstrate a tunable liquid waveguide bend. Unlike conventional diffusion processes [7,19,20,24,26], we use special boundary conditions to design the liquid bend. This diffusion method can generate a layered gradient RI profile that meets the requirements of TO bends. We have experimentally demonstrated 90° and 180° liquid bends in visible light, and the observed light propagations are consistent with the theoretical predictions. This work may broaden the areas of fluid dynamics and optics and have potential applications in tunable optical systems.

2. CONCEPT AND DESIGN

A. Physical Mechanism of Convection–Diffusion by Counterflow

Conventional convection–diffusion has been used for several microfluidic devices [7,19,24,26]. In this method, the input

liquids share the same flowing direction, leading to an inhomogeneous mixed medium where the flow moves forward. Here, we employ counterflows to build a new type of flow configuration [see Fig. 1(a)]. When one liquid moves radially outward whereas the other moves radially inward, the diffusion process can be almost uniform. For example, the counterflow has two flowing directions, radial direction (i.e., r or $-r$ direction) and tangential direction (i.e., θ direction). The level of diffusion in the θ direction is the same. This diffusion method is governed by the convection–diffusion equation [7]

$$\frac{\partial C}{\partial t} = D\nabla^2 C - U\nabla C + R, \tag{1}$$

where C is the concentration, D is the diffusion coefficient, U is the velocity, and R is the resource for a chemical species. On the right side of Eq. (1), the first item represents the diffusive transport process where the second item represents the convective transport process. For a steady-state flow, the solution concentration does not vary with time and no chemical reaction occurs between the two liquids, implying that $\partial C/\partial t = 0$ and $R = 0$. The RI of the mixed solution (n_c) is dependent on its concentration ($C \propto n_c^2$) [32]. Thus, from Eq. (1) we can obtain the formula when the flow velocity is close to 0 ($U \to 0$):

$$\nabla^2(n_c^2) = 0. \tag{2}$$

The RI profile derived from Eq. (2) is analogous to the profile generated by the QCTO [4], indicating that this diffusion method can meet the requirements of QCTO bends.

As shown in Fig. 1(a), the concentration at a point (r, θ) is formed by the interaction between the liquids injected in the θ_0 direction at t_0 and those injected in the $\theta_1, \theta_2, \theta_3, \ldots, \theta_n$ directions at $t_1, t_2, t_3, \ldots, t_n (n \to \infty)$, respectively. The concentration at point (r, θ) can be written as

$$C(r,\theta) = |C^1(r,\theta) + C^2(r,\theta)|_r + |C^1(r,\theta) + C^2(r,\theta)|_\theta, \tag{3}$$

where $C(r, \theta)$ is the concentration at point (r, θ), $C^1(r, \theta)$ and $C^2(r, \theta)$ are, respectively, the concentrations at (r, θ) caused by the glycol flow and water flow, and $|\,|_r$ and $|\,|_\theta$ represent the contribution in the r and θ directions, respectively.

The mass conservation equation in a rectangle is used [33]. For the liquid bends, the mass conservation equation in two orthogonal directions can be written as

$$U_r \frac{\partial C}{\partial r} = D\frac{\partial^2 C}{\partial r^2}, \qquad U_\theta r \frac{\partial C}{\partial \theta} = D\frac{\partial^2 C}{\partial \theta^2}, \tag{4}$$

where $r_1 < r < r_2$ (r_1 is the inner radius and r_2 the outer radius) and $0 \le \theta \le \pi/2$. U_r and U_θ represent the average velocity in the r and θ directions, respectively. In the r direction, there must be a concentration difference because of the two input lines [see Fig. 1(a)]. In the θ direction, the concentration is clear when $r = r_1$ or r_2. Substituting into Eq. (4) yields the result $\partial C/\partial\theta = 0$; in other words, the level of diffusion at a fixed r is identical, which is difficult to achieve using previous diffusion methods.

The ratio of diffusion and convection can be described by a non-dimensional number, the Péclet number, which can be

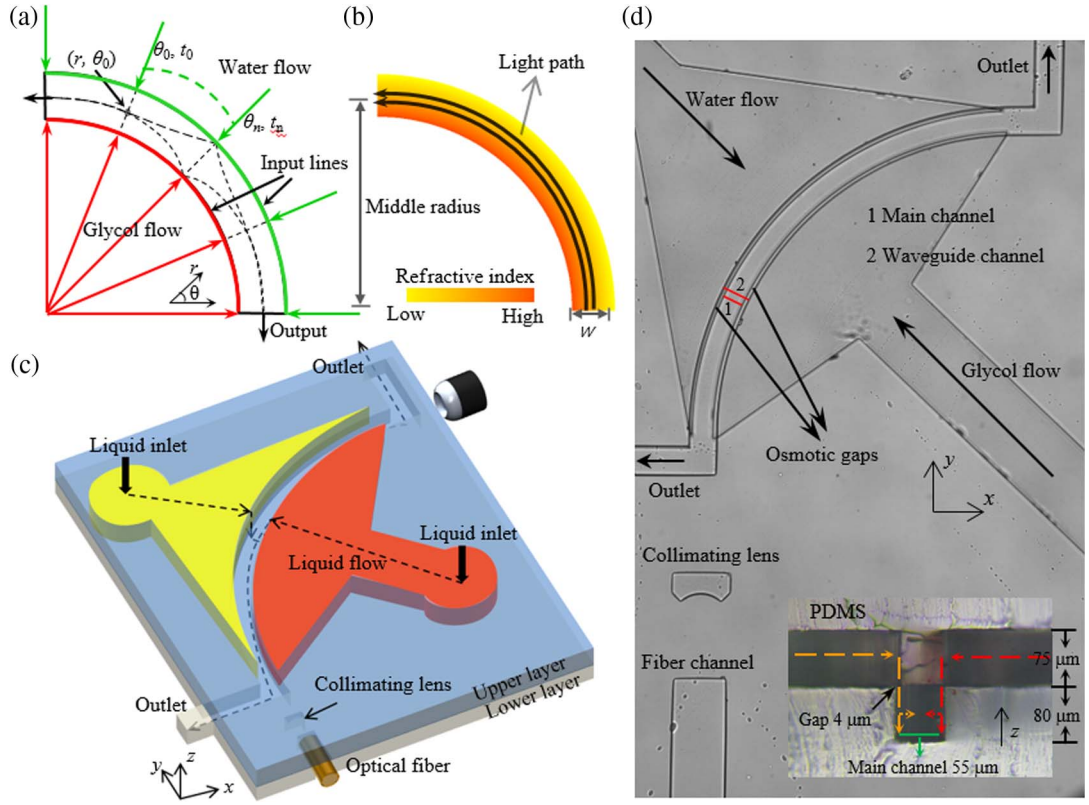

Fig. 1. Main concept of liquid waveguide bends. (a) Counterflow convection–diffusion process. The dotted black lines indicate the flowing direction. The concentration at a point contains different sources from different input positions. (b) Calculated RI profile (color map) as a result of the diffusion process in (a). The black arrows represent the light path. (c) Two-layer structure of the optofluidic device. The channel in the lower layer is the liquid transformation waveguide bends. (d) Top view of the fabricated chip. The inset shows the cross section at the middle of the bend, in which the red and yellow arrows represent the flowing directions of the glycol flow and water flow, respectively.

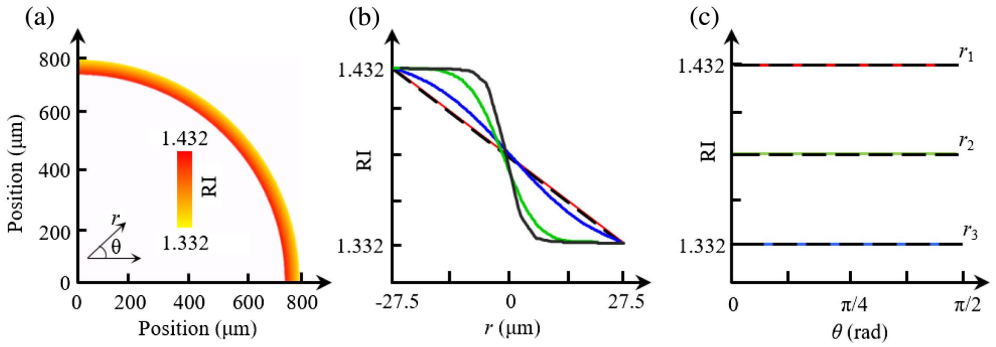

Fig. 2. Analysis of RI profile. (a) RI profile when the glycol flow rate is 16.84 nl/ min . (b) RI profile at the middle of the bend. The dotted black line represents the RI profile required by an ideal TO bend. The solid lines denote the RI profiles of the liquid bend when the glycol flow rate is 16.84 nl/ min (red), 50 nl/ min (blue), 100 nl/ min (green), and 200 nl/ min (black). The radii of –27.5, 0, and 27.5 μm represent r_1 (inner boundary), r_2 (middle radius), and r_3 (outer boundary), respectively. (c) RI profile at three different radii when the glycol flow rate is 16.84 nl/ min . The dotted black lines represent the RI profile for ideal TO bends. The solid lines are the RI profiles of the liquid bend at r_1, r_2, and r_3.

expressed as $Pe = (V_1 + V_2)W/D$, where W is the main channel width, and V_1 and V_2 are the velocities of the glycol flow and water flow, respectively. They have a limited relationship to ensure that the diffusion region is in the main channel. The velocity ratio V_2/V_1 should be about 2.5, and the ratio of the water flow rate and glycol flow rate (flow rate unit in nl/min) is 2.68. For fixed W and D, Pe can represent the level of diffusion between two liquids well. A small Pe indicates a low flow velocity and a high level of diffusion. In this case, the liquid bend has good performance.

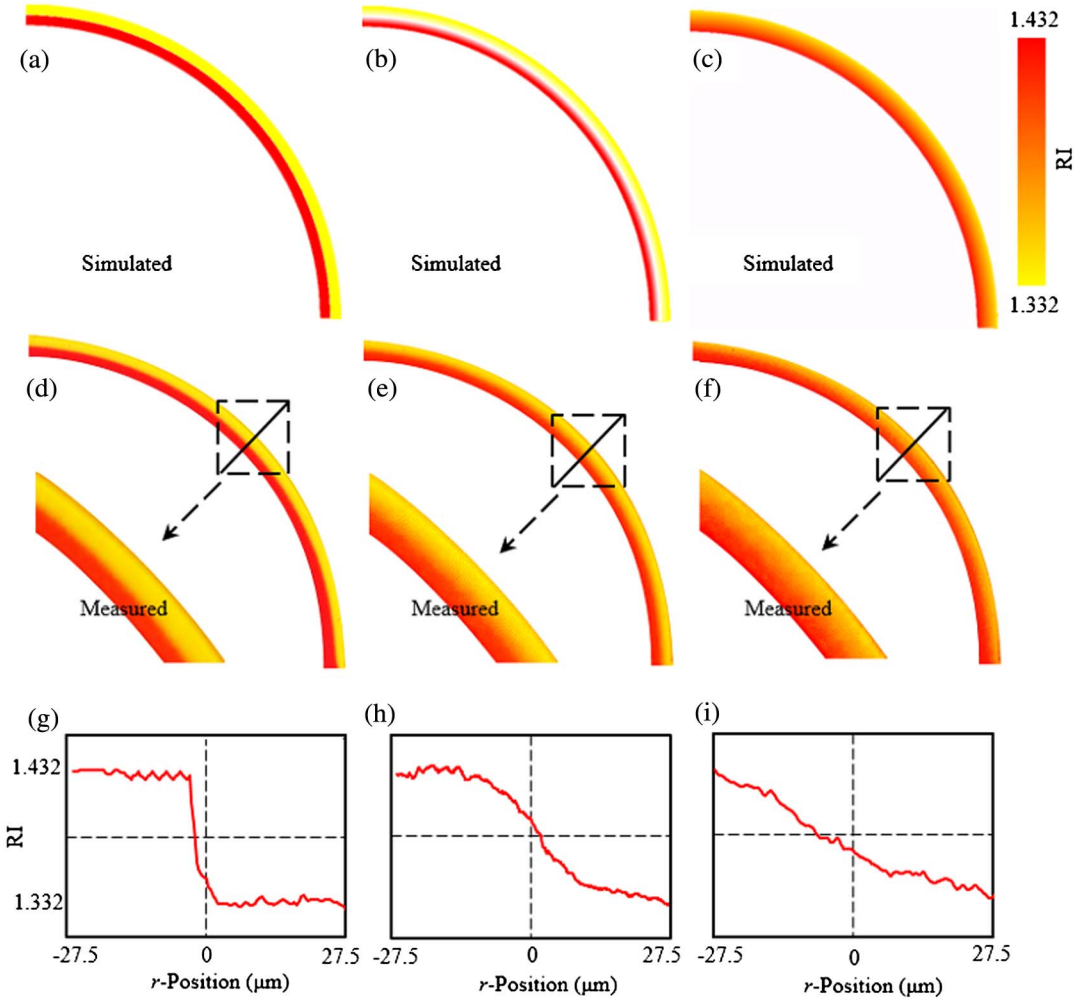

Fig. 3. Simulated and experimental RI profiles when the glycol flow rate is [(a), (d)] 449.14, [(b), (e)] 112.28, and [(c), (f)] 16.84 nl/ min . Panels (g), (h), and (i) show RI profiles along the solid black lines in (d), (e), and (f), respectively.

B. Device Design

The design of the liquid bends is illustrated in Fig. 1(c). The channel for diffusion is formed by a two-layer structure. The upper layer (75 μm high) has a fan-shaped area to inject and carry liquids, but has no waveguide channel or outlet, whereas the lower layer (80 μm high) has a waveguide channel and two outlets. The two layers are aligned and bonded together, as shown in Fig. 1(d), and there are osmotic gaps for the liquids to flow from the upper layer to the waveguide channel in the lower layer for convection–diffusion [see the cross section in the inset of Fig. 1(d)]. The inner input is injected with ethylene glycol ($n_{\text{gly}} = 1.432$), the outer input is injected with deionized (DI) water ($n_{\text{water}} = 1.332$), and the wall of the channel is polydimethylsiloxane (PDMS) ($n_{\text{PDMS}} = 1.410$). The boundaries of the channel are standard circular curves. The inner and outer radii of the channel are 741 and 804 μm, respectively. The width of the two osmotic gaps is 4 μm and the main channel width is 55 μm.

3. DEMONSTRATION FOR PROOF OF CONCEPT

A. Device Implementation

The two-layer structure of the device is fabricated using the standard soft lithography process with an accuracy of 2 μm. First, an SU-8 photoresist layer (MicroChem, SI8-50) is spin-coated onto a silicon wafer. After pre-baking, the master is exposed to UV light under a glass mask aligner. This treated master generates a positive bias-relief of the photoresist on the surface and can be used as a mold for the PDMS. A PDMS prepolymer is then poured over the master and stored in an oven for 1 h at 75°C. Then, the PDMS replica is peeled off from the master and processed by plasma oxidation to bond the upper and lower layers together. All liquids are stored in 100 μl glass syringes and driven by syringe pumps (Longer Pump, TS-1A). The liquids are transported from the pumps to the device by silicone tubes, and the needle tubing at the end of the silicone tubes is inserted into the reserved injection hole in the PDMS. A 532 nm green laser (CNI MGL-FN-532/1) is used as the light source; it is coupled to a single-mode optical fiber with NA = 0.12. The fiber can be inserted into the reserved channel [Figs. 1(c) and 1(d)]. A collimating lens between the fiber end and the waveguide channel is employed to collimate the fiber input to the waveguide channel [23,26,28,30].

B. Analysis of Refractive Index Distribution

In the liquid bend, the RI profile is determined by the level of diffusion between the two liquids. Figure 2(a) shows the RI profile when the glycol flow rate is 16.84 nl/min. In this case, the RI profile shows a linear relationship in the r direction [solid red line in Fig. 2(b)] and has the same level in the θ direction [solid lines in Fig. 2(c)], which match well with the required RI profiles of ideal TO bends [dashed black line in Figs. 2(b) and 2(c)]. With increase in glycol flow rates, the RI profile in the r direction differs from the desired RI profiles [see the solid blue, green, and black lines in Fig. 2(b)].

In Fig. 3, the glycol and water flows are represented in red and yellow, respectively. RI profiles corresponding to glycol flow rates of 449.14, 112.28, and 16.84 nl/min are presented in Figs. 3(a) and 3(d), 3(b) and 3(e), and 3(c) and 3(f), respectively. The experimental results [Figs. 3(d)–3(f)] match well with the simulated results [Figs. 3(a)–3(c)]. The RI profile at the middle of the bend fits closer to a linear function with decrease in glycol flow rate, as shown in Figs. 3(g)–3(i). Overviews of the experimental results can be seen in Fig. S5 of Supplement 1. Confocal images of the RI profiles are also presented to prove the homogeneity of the RI in the thickness direction (i.e., z direction) when the flowing condition is suitable for the liquid bend (see Fig. S6g of Supplement 1).

The dimensions of the liquid bend can be changed by varying the RI difference Δn between the liquids. For instance, when the radius is reduced, materials with a higher Δn can be chosen to realize the liquid bend (see Fig. S3a of Supplement 1).

C. Osmotic Mode Analysis

The limitation of the main channel height is also investigated. The liquid velocity from the osmotic gap to the channel bottom can be expressed by the following relationships:

$$\frac{1}{4}\cdot 2\pi r_1 \cdot a \cdot v_{\downarrow 1} = Q_1, \quad \frac{1}{4}\cdot 2\pi r_2 \cdot a \cdot v_{\downarrow 2} = Q_2. \tag{5}$$

The average velocity can be written as

$$\bar{v}_{\downarrow} = \frac{v_{\downarrow 1} + v_{\downarrow 2}}{2} = \frac{1}{\pi a}\left(\frac{Q_1}{r_1} + \frac{Q_2}{r_2}\right), \tag{6}$$

where a is the width of the osmotic gap, $v_{\downarrow 1}$ is the vertical speed of the glycol liquid from the gap to the channel bottom, $v_{v_{\downarrow 2}}$ is the vertical speed of the water liquid, Q_1 and Q_2 are, respectively, the glycol and water flow rates, and $\bar{v}_{\downarrow}$ is the average vertical speed of the two flows.

To obtain the maximum time for the liquids to arrive at the channel bottom from the osmotic gaps while still having a negligible influence on the level of diffusion in the horizontal direction, the relationships can be expressed as, respectively,

$$\frac{1}{4}\cdot 2\pi r_1 \cdot d_{\text{upper}} \cdot v_{\rightarrow 1} = Q_1, \quad \frac{1}{4}\cdot 2\pi r_2 \cdot d_{\text{upper}} \cdot v_{\rightarrow 2} = Q_2. \tag{7}$$

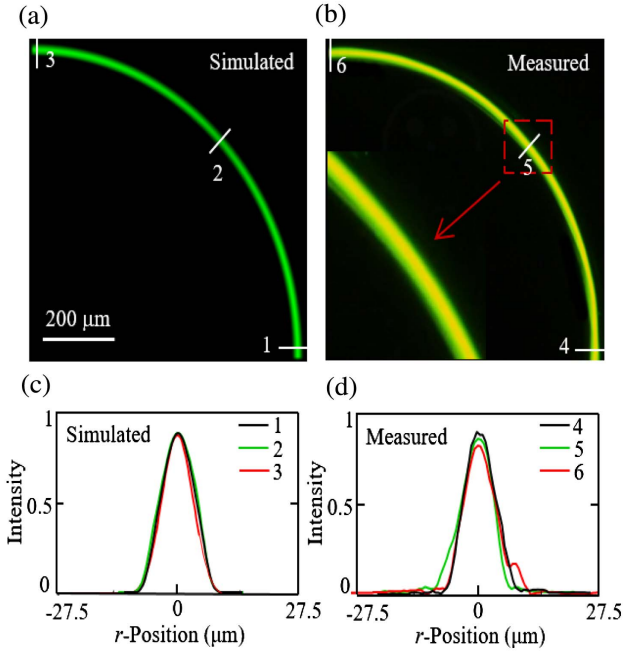

Fig. 4. Liquid bends of 90° at a glycol flow rate of 16.84 nl/min. Panels (a) and (b) show simulated and measured light propagation, respectively. Panels (c) and (d) show intensity profiles along the observation lines in (a) and (b), respectively. Line 1 (4) and 3 (6) represent the input and output, respectively.

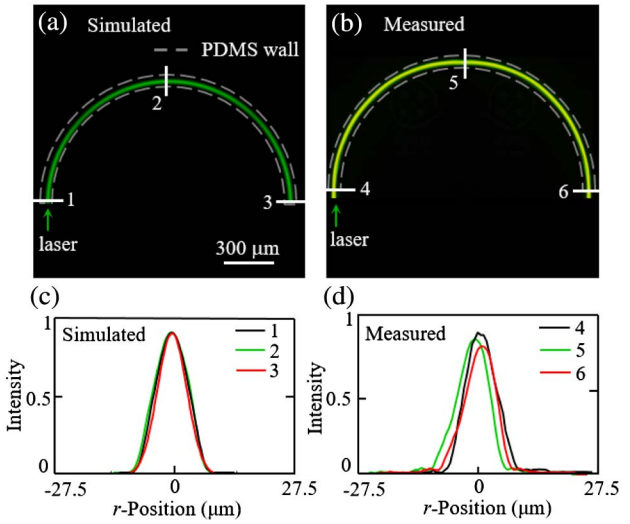

Fig. 5. (a) Simulated and (b) experimental light propagation in 180° liquid bends. Panels (c) and (d) show intensity profiles along the observation lines in (a) and (b), respectively.

If the flowing distance in the horizontal direction is s, we can obtain

$$v_{\rightarrow 1} t_{\rightarrow 1} = s, \qquad v_{\rightarrow 2} t_{\rightarrow 2} = s. \tag{8}$$

The average time $\bar{t}$ can be expressed as

$$\bar{t}_{\rightarrow} = \frac{t_{\rightarrow 1} + t_{\rightarrow 2}}{2} = \frac{s\pi d_{\text{upper}}}{4}\left(\frac{r_1}{Q_1} + \frac{r_2}{Q_2}\right), \tag{9}$$

where d_{upper} is the depth of the upper layer, $v_{\rightarrow 1}$ is the velocity of the glycol flow when it flows in the upper layer, $v_{\rightarrow 2}$ is the velocity of the water flow, $t_{\rightarrow 1}$ is the time that the glycol flow flows through s, and $t_{\rightarrow 2}$ is the time for the water flow.

When $s \le W/9$, the difference between the theory mode and the experimental osmotic mode is negligible. The relationship of the main channel height H can be written as

$$H = \bar{v}_{\downarrow}\bar{t}_{\rightarrow} = \frac{s d_{\text{upper}}}{4a}\left(2 + \frac{r_2 Q_1}{r_1 Q_2} + \frac{r_1 Q_2}{r_2 Q_1}\right), \tag{10}$$

where $s = W/9 = 6.11$ μm and $d_{\text{upper}} = 75$ μm. More details are presented in Fig. S2 of Supplement 1.

D. Simulated and Experimental Light Propagation

The intensity profile of the input light follows the Gaussian distribution $I = \frac{1}{\sigma\sqrt{2\pi}} I_0 \exp(-\frac{(r-r_0)^2}{2\sigma^2})$, the peak intensity I_0 is located at the middle radius position ($r_o = 0$), and the value of σ is the amplitude distribution ($4\sigma = W$). The factor $P = |r - r_o|/(0.5\ \text{W})$ is used to measure the movement of the peak intensity in the r direction. The absolute value of the coefficient r^2 (represented by a) is chosen to measure the deviation of the

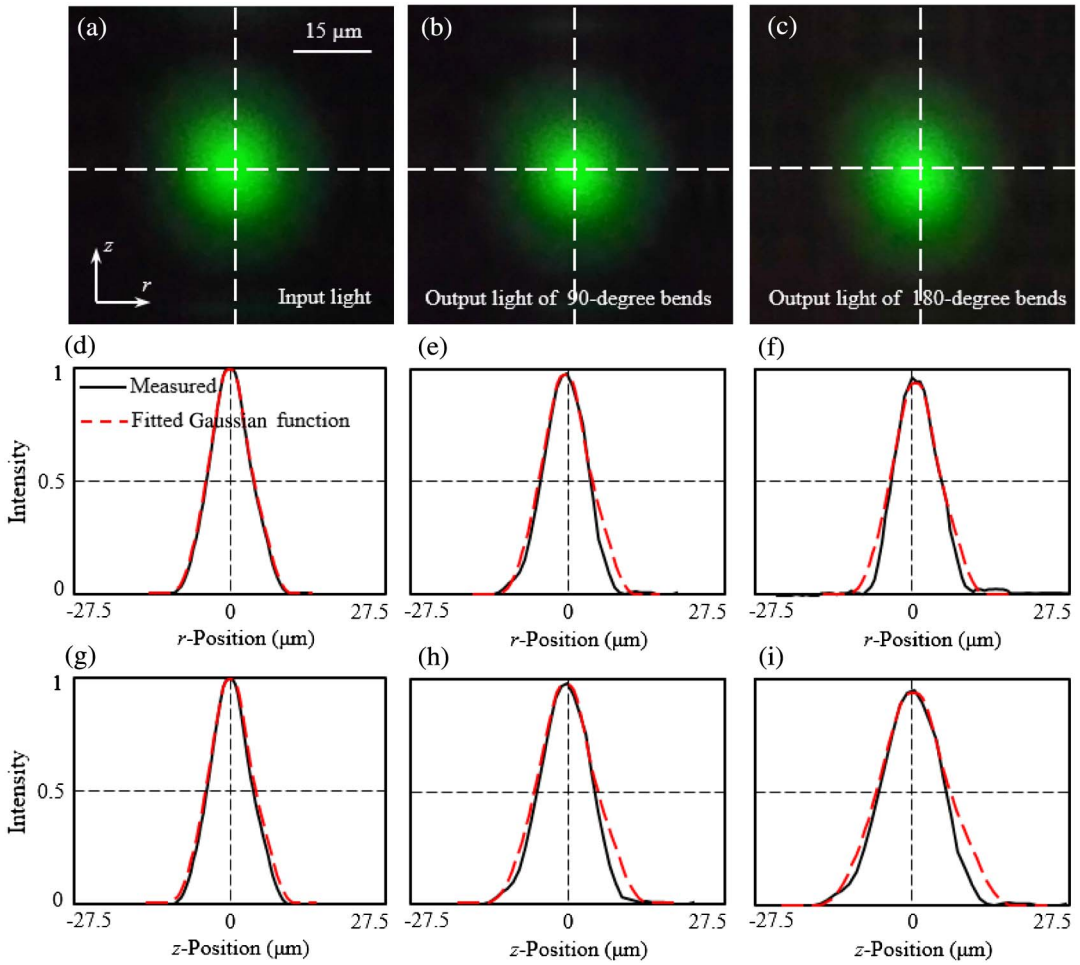

Fig. 6. Light beam profiles of the liquid bends. (a) Input and (b) output light of 90° bends, and (c) output light of 180° bends. Panels (d) and (g), (e) and (h), and (f) and (i) show light intensity profiles of (a), (b), and (c), respectively.

amplitude distribution $A = a/(0.5\sigma^2)$. Small A and P values represent the intensity profile at a reasonably high level of fidelity compared with large A and P values.

The fluorescent dye Rhodamine B is added into the liquids to visualize the light path (the concentration of Rhodamine B in both liquids is identical). The input light profile in all light experiments is identical and its position is also kept the same. The light intensity profiles are measured at the middle z plane ($z = 40$ μm). The liquid bend performs well when the glycol flow rate is 16.84 nl/min, as shown in Figs. 4(a) and 4(b). The intensity profiles along the observation lines in Figs. 4(a) and 4(b) are plotted in Figs. 4(c) and 4(d), respectively. The liquid bends can be modulated by changing the glycol flow rates (see Fig. S7 of Supplement 1 and Visualization 1). In Fig. 4(b), when line 1 is used as the reference, line 2 has $P = 0.01$ and $A = 0.05$ and line 3 has $P = 0.02$ and $A = 0.03$. This indicates that the intensity profile of the liquid bends is maintained well.

We also demonstrate the 180° bend. All the parameters (e.g., main channel width, middle radius, channel height, gap width, types of liquid, and flow rates) are identical to those of the 90° bend. The results are presented in Fig. 5 [simulation in (a) and experiment in (b)]. In Fig. 5(b), compared with line 4, $P = 0.04$ and $A = 0.02$ for line 5 and $P = 0.04$ and $A = 0.03$ for line 6. Again, this indicates that the 180° bend still works well.

The beam profiles of the output light are measured and shown in Fig. 6(b) (90° bends) and Fig. 6(c) (180° bends). Figure 6(a) is that of the input light. Figures 6(d) and 6(g), 6(e) and 6(h), and 6(f) and 6(i) show the intensity profiles of 6(a), 6(b), and 6(c), respectively. They indicate that the intensity profiles of the output light match well with the Gaussian function. The arbitrary profiles of the 90°, 180°, and 270° bends are simulated using the ray-tracing module (see Fig. 7). It can be observed that the beam profile is well maintained after different bending angles, further proving the good performance of the liquid bends.

The intensity is obtained by the emission light of the fluorescent dye. For a pure type of dye, the fluorescent intensity and laser intensity have a linear relationship; thus, the fluorescent intensity can represent the laser intensity [34,35]. The attenuation of light is calculated as $10\log_{10}(P_{\text{input}}/P_{\text{output}})$, where P_{input} is the power of the input light [line 4 in Figs. 4(b) and 5(b)] and P_{output} is the power of the output light [line 6 in Figs. 4(b) and 5(b)]. The bending loss in the liquid bends is negligible because of the characteristic of the TO design. Instead, the absorption by the fluorescent dye becomes dominant. In this work, the fluorescent dye is used to show the light path, but it is not necessary for real applications. Therefore, the bending loss is negligible for the liquid bends.

4. DISCUSSION

The experiments have demonstrated some merits of the liquid bends, for instance, tunable bending states and wide bending angles. The microfluidic system and supporting setups might be cumbersome in some applications; however, they can be removed if UV glues are used because the liquids and liquid bends are

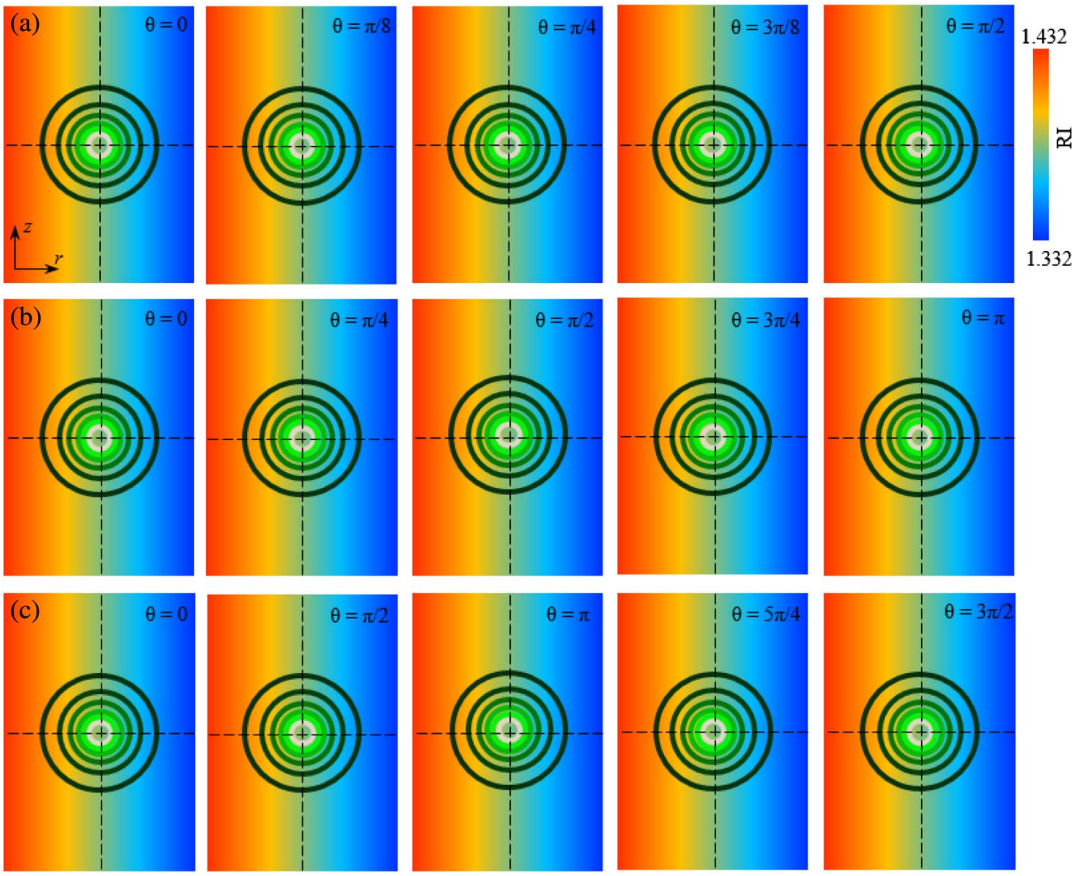

Fig. 7. Cross section of light in liquid bends using a ray-tracing module: (a) 90, (b) 180, and (c) 270° bends. $\theta = 0$ represents the input light. $\theta = \pi/2$, π, and $3\pi/2$ represent the output light.

cured to solidify after diffusion completion [36,37]. In addition, by using liquid diffusion, the liquid bends can naturally exhibit the other merits from the solid TO bend modes [12]. Here, we summarize this work. (1) A counterflow is employed to develop the diffusion process. The input directions (e.g., along r or $-r$ direction) are just one part of the flowing directions (e.g., along r, $-r$, and θ directions), generating nearly the same level of diffusion in the θ direction [see Figs. 2(a) and 2(c)]. This is a unique property compared with conventional diffusion methods [7,19,24]. (2) Liquids are continuous materials and can be used to change the RI continuously. This avoids the complicated fabrication of subwavelength structures [12–18]. (3) The bending angle can be even larger, such as 270° (see Fig. S8 of Supplement 1). This is already superior to solid waveguide bends, in which it is difficult to increase the bending angle to 180° while still maintaining good performance. (4) Most of the solid TO devices are limited to laboratory studies because of the reliance on metamaterials, the associated complex fabrication, and high cost [1,2,10,12]. In contrast, liquid bends use only common, low-cost liquids and the simple control of flow rates, making it easy to form the TO devices.

In conclusion, our work advances state-of-the-art QCTO by creating liquid-based waveguide bending systems. This is inspired by our new finding that the convection–diffusion process at low flow velocities can produce an RI profile analogous to QCTO. Liquid bends enable real-time tunable bending effects using the natural diffusion of miscible flows, while still showing the major merits of TO bends. The experiments have demonstrated 90° and 180° bends with good performance by using ethylene glycol and DI water as the liquid media. This work thoroughly demonstrates that the liquids are good choices for the TO devices. With rapid development of optofluidic technology, this device may be integrated into an optical communication system.

Funding. National Natural Science Foundation of China (NSFC) (61378093, 61377068); Open Foundation of National Laboratory for Marine Science and Technology (QNLM2016ORP0410); Natural Science Foundation of Hubei Province (2014CFA033); State Oceanic Administration, People's Republic of China.

Acknowledgment. We acknowledge the support from nanofabrication assistance from Center for Nanoscience and Nanotechnology at Wuhan University.

†These authors contributed equally to this work.

See Supplement 1 for supporting content.

REFERENCES

1. J. B. Pendry, D. Schurig, and D. R. Smith, "Controlling electromagnetic fields," Science **312**, 1780–1782 (2006).
2. D. Schurig, J. J. Mock, B. J. Justice, S. A. Cummer, J. B. Pendry, A. F. Starr, and D. R. Smith, "Metamaterial electromagnetic cloak at microwave frequencies," Science **314**, 977–980 (2006).
3. U. Leonhardt, "Optical conformal mapping," Science **312**, 1777–1780 (2006).
4. J. Li and J. B. Pendry, "Hiding under the carpet: a new strategy for cloaking," Phys. Rev. Lett. **101**, 203901 (2008).
5. S. Tretyakov, P. Alitalo, O. Luukkonen, and C. Simovski, "Broadband electromagnetic cloaking of long cylindrical objects," Phys. Rev. Lett. **103**, 103905 (2009).
6. J. Valentine, J. Li, T. Zentgraf, G. Bartal, and X. Zhang, "An optical cloak made of dielectrics," Nat. Mater. **8**, 568–571 (2009).
7. Y. Yang, A. Q. Liu, L. K. Chin, X. M. Zhang, D. P. Tsai, C. L. Lin, C. Lu, G. P. Wang, and N. I. Zheludev, "Optofluidic waveguide as a transformation optics device for lightwave bending and manipulation," Nat. Commun. **3**, 651 (2012).
8. J. W. Allen, H. Steyskal, and D. R. Smith, "Impedance and complex power of radiating elements under electromagnetic source transformation," Microw. Opt. Technol. Lett. **53**, 1524–1527 (2011).
9. C. Sheng, H. Liu, Y. Wang, S. N. Zhu, and D. A. Genov, "Trapping light by mimicking gravitational lensing," Nat. Photonics **7**, 902–906 (2013).
10. N. Kundtz and D. R. Smith, "Extreme-angle broadband metamaterial lens," Nat. Mater. **9**, 129–132 (2010).
11. M. Rahm, S. A. Cummer, D. Schuring, J. B. Pendry, and D. R. Smith, "Optical design of reflectionless complex media by finite embedded coordinate transformation," Phys. Rev. Lett. **100**, 063903 (2008).
12. D. A. Roberts, M. Rahm, J. B. Pendry, and D. R. Smith, "Transformation-optical design of sharp waveguide bends and corners," Appl. Phys. Lett. **93**, 251111 (2008).
13. M. Rahm, D. A. Roberts, J. B. Pendry, and D. R. Smith, "Transformation-optical design of adaptive beam bends and beam expanders," Opt. Express **16**, 11555–11567 (2008).
14. D.-H. Kwon and D. H. Werner, "Transformation optical designs for wave collimators, flat lenses and right-angle bends," New J. Phys. **10**, 115023 (2008).
15. N. I. Landy and W. J. Padilla, "Guiding light with conformal transformations," Opt. Express **17**, 14872–14879 (2009).
16. K. Yao and X. Jiang, "Designing feasible optical devices via conformal mapping," J. Opt. Soc. Am. B **28**, 1037–1042 (2011).
17. Z. L. Mei and T. J. Cui, "Experimental realization of a broadband bend structure using gradient index metamaterials," Opt. Express **17**, 18354–18363 (2009).
18. L. H. Gabrielli, D. Liu, S. G. Johnson, and M. Lipson, "On-chip transformation optics for multimode waveguide bends," Nat. Commun. **3**, 1217 (2012).
19. D. Psaltis, S. R. Quake, and C. Yang, "Developing optofluidic technology through the fusion of microfluidics and optics," Nature **442**, 381–386 (2006).
20. Y. Yang, L. K. Chin, J. M. Tsai, D. P. Tsai, N. I. Zheludev, and A. Q. Liu, "Transformation optofluidics for large-angle light bending and tuning," Lab Chip **12**, 3785–3790 (2012).
21. M. Ren, H. Cai, L. K. Chin, K. Radhakrishnan, Y. Gu, G.-Q. Lo, D. L. Kwong, and A. Q. Liu, "Coupled-ring reflector in an external cavity tunable laser," Optica **2**, 940–943 (2015).
22. Y. Sun and X. Fan, "Distinguishing DNA by analog-to-digital-like conversion by using optofluidic lasers," Angew. Chem. Int. Ed. **51**, 1236–1239 (2012).
23. W. Wu, X. Zhu, Y. Zuo, L. Liang, S. Zhang, X. Zhang, and Y. Yang, "Precise sorting of gold nanoparticles in a flowing system," ACS Photon. **3**, 2497–2504 (2016).
24. B. T. Mayers, D. V. Vezenov, V. Vullev, and G. M. Whitesides, "Arrays and cascades of fluorescent liquid—liquid waveguides: broadband light sources for spectroscopy in microchannels," Anal. Chem. **77**, 1310–1316 (2005).
25. Y. Yang, A. Q. Liu, L. Lei, L. K. Chin, C. D. Ohl, Q. J. Wang, and H. S. Yoon, "A tunable 3D optofluidic waveguide dye laser via two centrifugal Dean flow streams," Lab Chip **11**, 3182–3187 (2011).
26. Y. Shi, L. Liang, X. Q. Zhu, X. M. Zhang, and Y. Yang, "Tunable self-imaging effect using hybrid optofluidic waveguides," Lab Chip **15**, 4398–4403 (2015).
27. Y. C. Seow, A. Q. Liu, L. K. Chin, X. C. Li, H. J. Huang, T. H. Cheng, and X. Q. Zhou, "Different curvatures of tunable liquid microlens via the control of laminar flow rate," Appl. Phys. Lett. **93**, 084101 (2008).
28. Y. Shi, X. Q. Zhu, L. Liang, and Y. Yang, "Tunable focusing properties using optofluidic Fresnel zone plates," Lab Chip **16**, 4554–4559 (2016).
29. W. Song and D. Psaltis, "Electrically tunable optofluidic light switch for reconfigurable solar lighting," Lab Chip **13**, 2708–2713 (2013).
30. L. Liang, Y. F. Zuo, W. Wu, X. Q. Zhu, and Y. Yang, "Optofluidic restricted imaging, spectroscopy and counting of nanoparticles by evanescent wave using immiscible liquids," Lab Chip **16**, 3007–3014 (2016).

31. P. Fei, Z. Chen, Y. Men, A. Li, Y. Shen, and Y. Y. Huang, "A compact optofluidic cytometer with integrated liquid-core/PDMS-cladding waveguides," Lab Chip **12**, 3700–3706 (2012).
32. D. R. Lide, *Handbook of Chemistry and Physics*, 87th ed. (CRC Press, 2007), Chap. 8, p. 57.
33. E. L. Cussler, *Diffusion: Mass Transfer in Fluid Systems* (Cambridge University, 2009).
34. D. A. Walker, "A fluorescence technique for measurement of concentration in mixing liquids," J. Phys. E **20**, 217–224 (1987).
35. L. Li, X. Q. Zhu, L. Liang, Y. F. Zuo, Y. S. Xu, Y. Yang, Y. J. Yuan, and Q. Q. Huang, "Switchable 3D optofluidic Y-branch waveguides tuned by Dean flows," Sci. Rep. **6**, 38338 (2016).
36. C. Y. Tang, X. Zhang, Y. Chai, L. Hui, L. Tao, and Y. H. Tsang, "Controllable parabolic lensed liquid-core optical fiber by using electrostatic force," Opt. Express **22**, 20948–20953 (2014).
37. C.-Y. Tang, G. Bai, K. L. Jim, X. Zhang, K. H. Fung, Y. Chai, Y. H. Tsang, J. Yao, and D. Xu, "Lensed water-core Teflon-amorphous fluoroplastics optical fiber," J. Lightwave Technol. **32**, 1538–1542 (2014).